Hierarchical coupling effect in hollow Ni/NiFe₂O₄-CNTs microsphere via spray-drying for enhanced oxygen evolution electrocatalysis

Xuefeng Yu[1,§], Guanyu Chen[1,§], Yizhe Wang[2], Jiwei Liu[3], Ke Pei[1], Yunhao Zhao[1], Wenbin You[1], Lei Wang[1], Jie Zhang[1], Linshen Xing[1], Jingjun Ding[1], Guangzhou Ding[1], Min Wang[1] (✉), and Renchao Che[1] (✉)

[1] *Laboratory of Advanced Materials, Department of Materials Science and Collaborative Innovation Center of Chemistry for Energy Materials (iChem), Fudan University, Shanghai 200438, China*

[2] *Materials Genome Institute, International Centre of Quantum and Molecular Structures, and Physics Department, Shanghai University, Shanghai 200444, China*

[3] *College of Materials and Environmental Engineering, Hangzhou Dianzi University, Hangzhou 310012, China*

[§] *Xuefeng Yu and Guanyu Chen contributed equally to this work.*

ABSTRACT

Design and fabrication of cost-effective transition metal and their oxides-based nanocomposites are of paramount significance for metal-air batteries and water-splitting. However, the traditional optimized designs for nanostructure are complicated, low-efficient and underperform for wide-scale applications. Herein, a novel hierarchical framework of hollow Ni/NiFe₂O₄-CNTs composite microsphere forcibly-assembled by zero-dimensional (0D) Ni/NiFe₂O₄ nanoparticle (< 16 nm) and one-dimensional (1D) self-supporting CNTs was fabricated successfully. Benefitted from the unique nanostructure, such monohybrids can achieve remarkable oxygen evolution reaction (OER) performance in alkaline media with a low overpotential and superior durability, which exceeds most of the commercial catalysts based on IrO_2/RuO_2 or other non-noble metal nanomaterials. The enhanced OER performance of Ni/NiFe₂O₄-CNTs composite is mainly ascribed to the increased catalytic activity and the optimized conductivity induced by the effects of strong hierarchical coupling and charge transfers between CNTs and Ni/NiFe₂O₄ nanoparticles. These effects are greatly boosted by the polarized heterojunction interfaces confirmed by electron holography. The density functional theory (DFT) calculation indicates the epitaxial Ni further enriches the intrinsic electrons contents of NiFe₂O₄ and thus accelerates absorption/desorption kinetics of OER intermediates. This work hereby paves a facile route to construct the hollow composite microsphere with excellent OER electrocatalytic activity based on non-noble metal oxide/CNTs.

KEYWORDS

spray-drying, novel structure, oxygen evolution reaction (OER), electron holography, composite microsphere

1 Introduction

An urgent issue of energy consumption and environmental pollution has been focused on gradually, which asks greatly for the exploitation and development of new energy storage and conversion devices [1]. As a key half reaction, the oxygen evolution reaction (OER) plays essential roles on them, especially in rechargeable metal-air batteries and water-splitting [2, 3]. However, caused by the multiple proton-coupled electron transfer process, the sluggish kinetics always dominates which results in high overpotential and considerable energy loss [4, 5]. As the most efficient OER catalyst, the noble metal-based nanomaterials such as ruthenium/iridium have been researched widely and available commercially [6, 7]. Unfortunately, the high expenses, limited earth resources and poor stability still exist, which hinder extremely their industrial application [8, 9]. For further decreasing costs and increasing benefits, therefore, there have been intensive demands for substitutions endowed with excellent OER activities to replace noble metal-based nanomaterials [10, 11].

More recently, the transition metal and their oxides-based nanocomposites have received tremendous attention which is considered as a promising alternative for OER because of the rich abundance, low-spending and unique electronic structure [12, 13]. Numerous efforts, for example decreasing nanoparticle sizes, designing microscopic morphology, doping additional metal or nonmetallic elements, introducing rich defects have been devoted to fabricate the benign OER electrocatalyst [14–17]. In particular, many typical transition metal and their oxides-based nanocomposites such as the morphous F-doping $SrCoO_{3-\sigma}$ [18], $TaO_2F/^gC$ [19], $CuFe_2O_4/PCFs$ [20], 3D Co@N/C [21], $CoTe_2@NCNTFs$ [22], Co-Fe-Bi/NF [23], mesoporous NiFe₂O₄ nanorods [24] and so on, were successfully prepared. As expected, the reduced overpotential and Tafel slope have been achieved to some extent. Despite these great advances, the main enhanced obstacles, in light of the poor conductivity and limited catalytic sites still remain, which slow the development of catalytic activities down. In response to these, currently, the heterogeneous interface engineering become more and more fashionable to regulate the intrinsic electron structure of active sites reported by Driess et al. [25–27]. Nevertheless, the direct microscope observation for the electron transfer along

---

with the heterojunction interface is of huge insufficiency that prevents a deep insight into the OER mechanism.

As well known, a rational structure design is more conducive to achieve the large specific surface, good conductivity, thus to expose more activity sites and to accelerate the electrocatalysis kinetics [28–30]. According to a large number of researched literatures, however, some difficulties for nanostructure optimization must be resolved to further perfect the correlation between nanostructure and performance of the transition metal and their oxides based composites [31–34]. i) The structure synergy between components should be considered to improve conductivity and stability. ii) The loading amount of active nanoparticles on the surface of composites should be raised for more beneficial catalysis. iii) The diameter sizes of the active nanoparticles should be further reduced for more exposed active sites. iv) What's more, the electron transfer of composites could be influenced by the intrinsic magnetic field due to the Lorentz force [35, 36]. The relevant microscopy description for electromagnetic coupling effect is still a big challenge. v) More importantly, the traditional synthesis methods of the transition metal and their oxides-based composites are always complex, low yield, high cost, preventing their practical application [37, 38]. Apparently, to design a novel transition metal and their oxides-based composites endowed with more efficient nanostructure synergy and to study the hierarchical interface coupling effect deeply are of great significance to improve OER performance and understand the mechanism.

Herein, for the first time, a novel nanostructure of hollow Ni/NiFe$_2$O$_4$-CNTs composite microsphere has been constructed via a facile forcibly-assembled method. A great deal of Ni/NiFe$_2$O$_4$ nanoparticles (< 16 nm size) are uniformly confined onside the surface of the hollow CNTs self-supporting shell. In case of the hierarchal coupling effects and optimized synergy, the conductivity and the electrocatalytic activity of composite are extremely improved, thus achieving the highlighted OER performance. The overpotential at a current density of 10 mV/cm^2 has been reduced to 1.541 V (vs. RHE) in alkaline with superior durability, which surpasses most of the traditional catalysts based on IrO$_2$/RuO$_2$ and other non-precious nanocomposites. Electron holography confirms that the polarized heterojunction interfaces greatly promote the charge redistribution and favor them to transfer from CNTs to Ni/NiFe$_2$O$_4$ nanoparticles. Also, the density functional theory (DFT) calculation describes that the epitaxial Ni of Ni/NiFe$_2$O$_4$ nanoparticles can further provide richer electrons to NiFe$_2$O$_4$. The accumulated electrons can weaken the Fe-O bonds of NiFe$_2$O$_4$ during the catalytic process, and accelerate the absorption/desorption kinetics of OER intermediates [39–41]. Moreover, the intrinsic magnetic field originating from Ni/NiFe$_2$O$_4$ has completely penetrated through Ni/NiFe$_2$O$_4$-CNTsHMS, which can affect the electron/charge transfer by the Lorentz force. Our results thereby lay a foundation for the design of unique transition metal oxides based OER catalysts and give insight into the catalytic mechanism.

2   Experimental

2.1   Chemicals

Nickel(II) acetate tetrahydrate, iron(III) nitrate nonahydrate, carbon nanotubes dispersion solution (TNWDM-M8), potassium hydroxide were acquired from Sinopharm Chemical Reagent Co., Ltd, which were of analytical grade and could be directly used without purification. Notably, the carbon nanotubes dispersion solution is mainly composed of CNTs (TNM8) and TNWDIS dispersant. Deionized water (DI) water consumed in here was got from a Milli-Q system (Millipore, Bedford, MA).

2.2   Synthesis of 3D Ni/NiFe$_2$O$_4$-CNTs hybrid microspheres

The hollow Ni/NiFe$_2$O$_4$-CNTs composite microsphere with hierarchical nanostructure and yarn-ball like morphology was synthesized via a facile forcibly-assembled spray-drying process followed by calcination. Briefly, 1 g of nickel(II) acetate tetrahydrate and 0.5 g iron(III) nitrate nonahydrate were dissolved respectively into a stable solution mixed by 20 mL distilled water and 50 mL CNTs dispersion solution. With a continuous stirring for 7 h, the transparent solution above was transformed into a spray-drying device, where it was broken up to a spray of small droplets. By the strong hot stream, these droplets would be rapidly evaporated, resulting in a great deal of the dried powders which then were collected from the separated equipment by centrifugal force. The responding temperatures of inlet and outlet sites of the spray dryer were set at 180 ºC and 90 ºC, respectively. Finally, the as-fabricated powders were obtained by subsequent post-treatment under Ar atmosphere at 600 ºC for 3 h, denoting herein as Ni/NiFe$_2$O$_4$-CNTsHMS. In addition, the synthesis method of 3D Ni-CNTs hybrid microspheres, Fe$_2$O$_3$-CNTs hybrid microspheres and CNTs hybrid microspheres is similar as Ni/NiFe$_2$O$_4$-CNTsHMS without the addition of iron salts, nickel salts and both of them, which we name as Ni-CNTsHMS, Fe$_2$O$_3$-CNTsHMS and CNTsHMS, respectively.

2.3   Characterization

The crystallographic structure was characterized by X-ray diffraction (XRD) which is equipped by Ni-filtered Cu Kα radiation (Bruker). The carbon content was calculated by Thermogravimetric analysis burned from 25 to 900 °C with heating rate of 10 °C/min in air (Pyris 1 TGA-207). The Ni/Fe molar ratio was calculated by inductively coupled plasma-optical emission spectroscopy (ICP-OES). Before test, the sample was firstly dissolved in 3:1 v/v HCl: HNO$_3$ (conc.) and then diluted to ca. 400 ppb in 2% HNO$_3$ v/v. The defective information of carbon was researched by the Raman spectra with a 633 nm laser excitation. The size and morphology were observed by field emission scanning electron microscope (FESEM) (Hitachi S-4800, Japan) and transmission electron microscope (TEM) (JEOL JEM-2100F). Many characterizations of high resolution transmission electron microscope (HRTEM), selected area electron diffraction (SAED), electron energy loss spectroscopy (EELS), energy dispersive spectroscopy (EDS), scanning TEM (STEM)-element-mapping and even electron holography were implemented on TEM (JEOL JEM-2100F) design with a post-column Gatan imaging filter (GIF-Tridium). The magnetic properties were investigated by a SQUID magnetometer (Quantum Design Company of USA). The Specific surface area and pore properties were analyzed by ASAP 2420 analyzer at 77 K. Moreover, the characterization of X-ray photoelectron spectroscopy (XPS) (ESCALAB210) could be applied for clarifying the chemical composition and elemental states of samples.

2.4   Electrocatalytic measurement

The electrocatalytic activities for the OER were evaluated by electrochemical Workstation (CHI 760D). Based on the ring-disk electrode (RDE) techniques, all electrochemical measurements were finished in a standard three electrodes system at 300 K. A glassy carbon (GC) disk electrode coated with Ni/NiFe$_2$O$_4$-CNTsHMS or other samples was chose as the

working electrode. Meanwhile, the Hg/HgO electrode and a carbon rod were used as the reference and counter electrodes, respectively.

Firstly, the samples of 5 mg were dispersed in a stable solution under sonication, which mixed with 0.8 mL of water, 0.2 mL of ethanol and 40 μL of 5 wt.% Nafion. The homogeneous catalyst ink (10 μL) obtained above was dropped onto the GC electrode with natural drying for the preparation of the working electrode. Before the test, the steady voltammogram curves were achieved by repeated scans from 0 to 0.8 V (vs. Hg/HgO). Afterwards, the linear sweep voltammetry (LSV) was obtained in the range between 1.3 and 1.7 V (vs. RHE) at 5 mV/s in N_2-saturated 1 M KOH solution at rotation speed of 1,600 rpm. Notably, all potentials were shown by the converted RHE values according to the followed equation: E (RHE) = $E_{Hg/HgO}$ + 0.098 + 0.0591pH. Furthermore, all the polarization plots were calibrated based on the equation: $E_{corrected} = E - iR$, in which i is the current and R is the uncompensated ohmic electrolyte resistance. For evaluating OER kinetic performance, the Tafel plots were implemented by repotting overpotential versus log current. According to the Tafel equation ($\eta = a + b\log(j)$), the Tafel slope (b) was thus drown by fitting the linear part of the Tafel plots. The activity surface areas of the composites were determined by electrochemical active surface area (ECSA) which is proportional to electrochemical capacitance. The electrochemical capacitance could be measured using cyclic voltammetry (CV) with different scan rates, which was generally chose to the non-Faradic current region at the CV potential ranges. The different scan rates were applied by 4, 8, 12, 16 and 20 mV/s. Correspondingly, the ECSAs of all these samples could then be calculated via dividing C_{dl} by the specific capacitance as shown in the following equation: ECSA = C_{dl}/C_s, which was often used of 40 μF/cm^2 (C_s) for metal oxide.

3　Results and discussion

The synthesized process of Ni/NiFe$_2$O$_4$-CNTsHMS has been schematically illustrated in Figs. S1 and S2 in the Electronic Supplementary Material (ESM). At first, the iron nitrate: nickel acetate (mass ratio = 1:2) and CNTs dispersion solution were homogenously dispersed in DI water. Afterwards, the stable solution was transferred into a specialized spray instrument, which was broken up to generate a great deal of tiny droplets mainly consisted of iron ions, nickel ions, functional CNTs, and water molecules. The relevant parameters of the experiment were shown in Figs. S1 and S2 in the ESM. Under the heat exchange of hot wind stream, water molecules evaporated quickly and these ions were captured by functional CNTs. Notably, the diffuse speed of water molecules and ions outward was extremely rapid than that of CNTs inward. By virtue of the strong self-supporting effect of CNTs, the huge cavity was generated and the composite microspheres thus were endowed with forced assembly structure. Finally, calcined under Ar atmosphere at 600 °C, the hollow Ni/NiFe$_2$O$_4$-CNTsHMS was obtained, the surface of which was anchored uniformly by a mass of Ni/NiFe$_2$O$_4$ nanoparticles with the size of less than 16 nm.

Figure 1(a) exhibits the crystal phase structure for our samples. The typical diffraction peak appearing at 26° for CNTsHMS was assigned to (002) plane of hexagonal graphite carbon [42]. For Ni-CNTsHMS, in addition to the peak of graphite carbon, the sharp diffraction peaks of 44.8°, 52.08° and 76.6° can match well with the (111), (200), and (220) reflections of metallic nickel (JCPDS Card No. 04-0850), respectively [43]. Obviously, the nickel oxide decomposed from nickel acetate is not stable and can be reduced under Ar atmosphere at 600 °C. In contrast, iron oxide still remains original. These peaks of Fe$_2$O$_3$-CNTsHMS are mainly ascribed to γ-Fe$_2$O$_3$ also proved by the classic interlayer distance of 0.48 nm (JCPDS Card No.19-0629) (Fig. S3 in the ESM). Interestingly, when the mass ratio of nickel acetate and iron nitrate is about 2, the Ni/NiFe$_2$O$_4$-CNTsHMS seems to show the similar peaks as Fe$_2$O$_3$-CNTsHMS. However, after careful analysis (Fig. 1(b)), these peaks of 18.81°, 30.65°, 36.07°, 44.38°, 54.09°, 57.39°, 63.04°, 74.94° have shifted positively than that of Fe$_2$O$_3$-CNTsHMS,
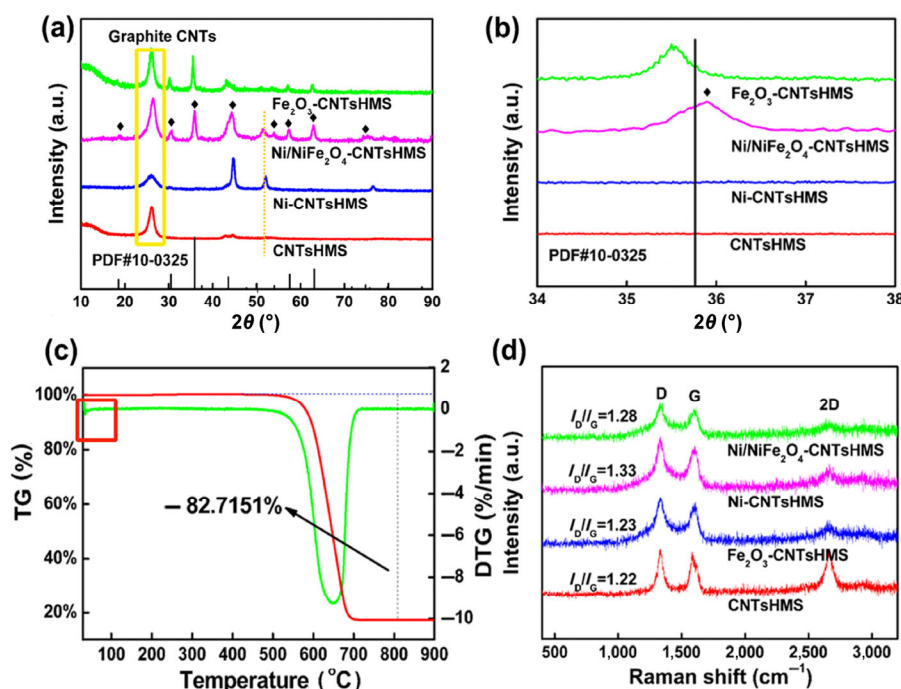

Figure 1　(a) and (b) XRD patterns of the CNTsHMS, Ni-CNTsHMS, Fe$_2$O$_3$-CNTsHMS and Ni/NiFe$_2$O$_4$-CNTsHMS. (c) TG-DTG curves of the Ni/NiFe$_2$O$_4$-CNTsHMS (the carbon content of Ni/NiFe$_2$O$_4$-CNTsHMS is estimated to 82.7151%. Correspondingly, the total metal oxides content of Ni/NiFe$_2$O$_4$-CNTsHMS is evaluated to 17.29%). (d) Raman spectra of the CNTsHMS, Ni-CNTsHMS, Fe$_2$O$_3$-CNTsHMS and Ni/NiFe$_2$O$_4$-CNTsHMS (the peak intensity ratio is derived from the mathematically integral area).

and correspond well to inverse spinel $NiFe_2O_4$ (JCPDS Card No.10-0325). The transformation reason for $NiFe_2O_4$ is believably attributed to the direct chemical reaction between NiO and γ-Fe_2O_3. The redundant nickel atoms are then reduced by CNTs to form the epitaxial metal Ni (Tables S1 and S2 in the ESM). The expanded θ values for $NiFe_2O_4$ and the reduced value for Ni at 51.4° may be caused by the atomic mutual migration at heterojunction interfaces of Ni/$NiFe_2O_4$ NPs. The corresponding component content of Ni/$NiFe_2O_4$ was detected by ICP-OES in Table S1 in the ESM. In the composites, the atomic molar ratio of Ni:Fe is estimated to be 1.45 and the molar ratio of Ni:$NiFe_2O_4$ could be calculated to be 1.9 (Table S1 in the ESM). According to the result of TGA (Fig. 1(c)), the content of CNTs in Ni/$NiFe_2O_4$-CNTsHMS has reached to 82.71%. Therefore, in case of the total metal oxides content of 17.29%, other component content of catalyst can be calculated to 5.072% for Ni loading and 10.796% for $NiFe_2O_4$ loading (Table S2 in the ESM). Marked by red frame, the oxidation process of Ni metal has taken place at about 70 °C because of the high specific surface energy. Moreover, the DTG curve indicates that the combustion of CNTs mainly occurs at 650 °C. The graphitization degree of CNTs-based composites was investigated by Raman spectra (Fig. 1(d)). The sharp peaks of 1,350, 1,593, and 2,692 cm^{-1} represent the D, G and 2D band, respectively. The characteristic D and G bands are related to the disordered or defected carbon and graphitic sp^2-carbon while the 2D band is a characteristic feature of high-quality graphene [44]. Due to the introducing of metal precursors, the 2D peak intensity of Ni-CNTs HMS, Fe_2O_3-CNTsHMS and Ni/$NiFe_2O_4$-CNTsHMS is lower than pure CNTsHMS, which

elaborates the strong interaction between metal and CNTs. The more comprehensive information can be further investigated by the intensity ratio of the D and G peaks. Clearly, with the more content of nickel element adding the total defect degree of composites shows an increasing tendency. For Ni/$NiFe_2O_4$-CNTsHMS, the abundant defects caused by excess nickel element are in favor of regulating the adsorption state of OER intermediates and thus facilitate the OER kinetic process [45].

Figure 2(b) and Fig. S4 in the ESM exhibit a hollow, well-dispersed, yarn-ball like morphology for as-fabricated Ni/$NiFe_2O_4$-CNTsHMS. The corresponding sizes of microparticles are measured from 2.5 to 24 μm (Fig. S5(a) in the ESM). Focused on the detailed images of a single microsphere (Figs. 2(c) and 2(d), and Fig. S6 in the ESM), the surface of the composite microsphere is self-assembled by a great deal of self-supporting CNTs. A mass of nanoparticles less than 16 nm diameters was embedded uniformly onside the surface of hollow self-supporting CNTs shell (The enlarged images shown in Figs. 2(e) and 2(f), and Fig. S5 in the ESM). Figures 2(g)–2(i) show the TEM pictures of Ni/$NiFe_2O_4$-CNTsHMS. The complicated 3D nanostructure is self-fabricated by zero-dimensional (0D) nanoparticles and one-dimensional (1D) CNTs. The lattice interlayer distances of nanoparticles are measured of 0.482 and 0.241 nm, which matches well with the transition metal oxides $NiFe_2O_4$ (111) and (222) planes (Fig. 2(i)). The other lattice interlayer distances of 0.176 and 0.208 nm are mainly ascribed to the metal Ni (200) planes and the transition metal oxides $NiFe_2O_4$ (400) planes. The similar heterojunction interfaces composed of epitaxial Ni and $NiFe_2O_4$ are also observed on other crystal planes sequences such as (200) for Ni and (222) for $NiFe_2O_4$ or
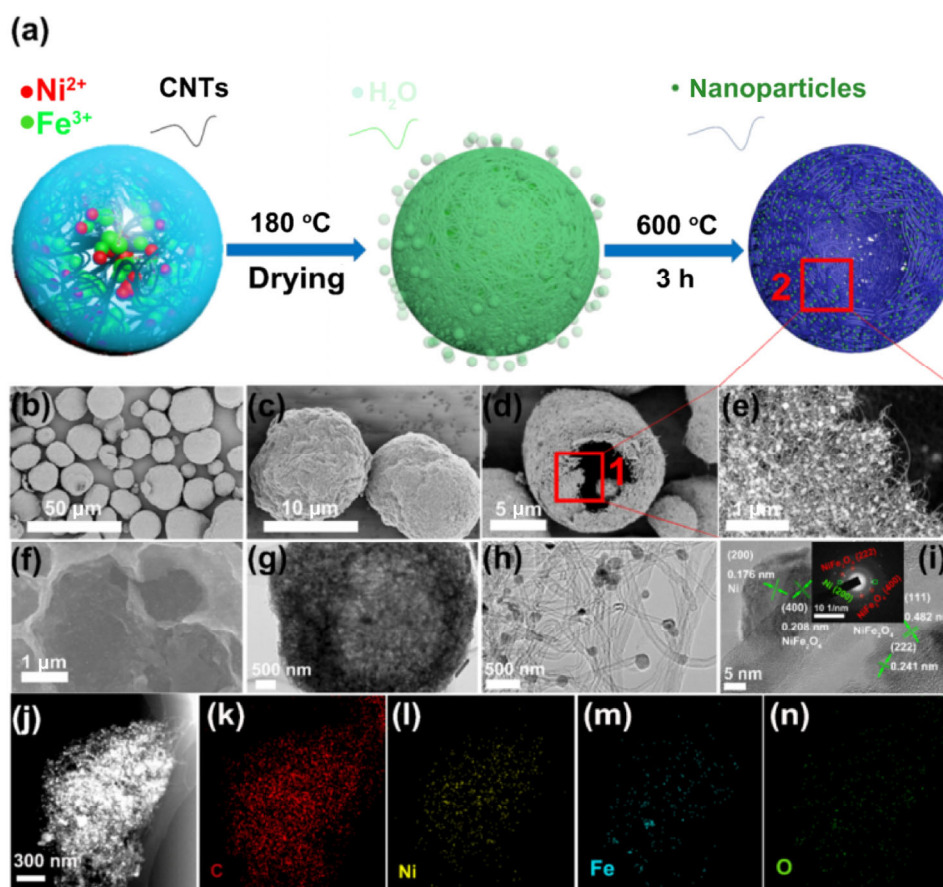
**Figure 2** (a) Simplified schematic illustration of the formation processes of prepared Ni/$NiFe_2O_4$-CNTsHMS. (b)–(d) SEM images of Ni/$NiFe_2O_4$-CNTsHMS. (e) FFSEM images of Ni/$NiFe_2O_4$-CNTsHMS. (f) FFSEM image of the cross-section of Ni/$NiFe_2O_4$-CNTsHMS by ultra-thin section technique. (g) and (h) TEM images of Ni/$NiFe_2O_4$-CNTsHMS. (i) HRTEM and SAED images of Ni/$NiFe_2O_4$-CNTsHMS. The STEM-Mapping images of the part area of Ni/$NiFe_2O_4$-CNTsHMS by ultra-thin section technique. (j) STEM picture, (k) C, (l) Ni, (m) Fe, (n) O.

(111) for Ni and (511) for NiFe₂O₄ (Fig. S7 in the ESM). Also confirmed by SEAD (the inset picture of Fig. 2(i)), metal Ni and transition spinel metal oxides NiFe₂O₄ coexist in the composites. Both the high-angle annular dark field (HAADF)-STEM-mapping and element mapping images of SEM reveal that the Ni, Fe, O elements all dispersed homogenously on the surface of the 3D CNTs self-supporting framework (Figs. 2(j)–2(n) and Fig. S8 in the ESM). Whereby, the Ni/NiFe₂O₄-CNTsHMS characterized with the yarn-ball like morphology and hierarchal nanostructure was successful synthesized. Strikingly, with the 3s spray-drying process followed with post-annealing, a series of hollow CNTs self-supporting composite microspheres, for instance Ni-CNTsHMS, Fe₂O₃-CNTsHMS and CNTsHMS, can be fabricated, which reveals the universality of our strategy (Fig. S9 in the ESM). Moreover, in comparison to the traditional chemical synthesis, the pray-drying route is facile, low-cost, large output, and beneficial for the industrial production (Fig. S10 in the ESM).

The magnetic properties of hybrid composites were evaluated by vibrating sample magnetometer (VSM) measurements (Figs. 3(a) and 3(b)). As a result, the Ni/NiFe₂O₄-CNTsHMS have achieved the largest coercivity and secondary saturation magnetization. It is induced by the controlled synergy of the magnetic anisotropy, crystal size and defect degree of Ni/NiFe₂O₄-CNTsHMS, which may play a critical role to affect catalytic performance [46, 47]. Figures 3(c) and 3(d) show nitrogen absorption/desorption isotherm and the corresponding pore properties of Ni/NiFe₂O₄-CNTsHMS. Attributed to the self-supporting effect of CNTs, the specified surface area of Ni/NiFe₂O₄-CNTsHMS is measured of 77.3 m²/g and the hierarchical nanopores are included by micropores, mesoporous, macropores (Figs. 3(c) and 3(d)). Compared with spinel NiFe₂O₄ or NiFe₂O₄-based composites, the Ni/Fe₂O₄-CNTsHMS shows larger surface area and richer nanopores (Table S3 in the ESM) [48–53]. Therefore, the forcedly-assembled method by spray-drying is favorable to expose more active sites, to boost mass transfer process of electrolytes, and ultimately to enhance the OER performance.

The wide XPS spectrum (Fig. 4(a)) unravels the Fe, Ni, O, C elements have coexisted onside the surface of Ni/NiFe₂O₄-CNTsHMS. No other impurity elements are detected in here, which confirms the purity of our composite. The fitted Ni 2p spectrum (Fig. 4(b)) could be divided into two spit-orbit peaks located at 874 and 856 eV. They can be assigned to the Ni 2p₁/₂ and Ni 2p₃/₂, respectively. The corresponding shakeup peaks (880 eV for Ni 2p₁/₂, sat. and 862 eV for Ni 2p₃/₂, sat.) can be identified as Ni satellite peaks of NiO, demonstrating the oxidation state of Ni²⁺ cation ions onside the surface of Ni/NiFe₂O₄ NPs [54, 55]. On the one hand, it is helpful for decreasing nanomaterial resistance and accelerating charge/electron transfer between CNTs and nanoparticles. On the other hand, the lost electrons of metal Ni mainly have transferred to NiFe₂O₄ which enriches the intrinsic electrons contents of it confirmed by later DFT calculation. Strikingly, the typical peak of 852 eV is ascribed to the Ni metal agreeing with the results of XRD and HRTEM [56]. The fitted Fe 2p spectrum (Fig. 4(c)) shows two spit-orbit peaks of Fe 2p₁/₂ at 725 eV and Fe 2p₃/₂ at 711 eV, and no satellite peaks at 719 and 732 eV are observed because of no separate hematite phase [57]. The special peak at binding energy of 707.5 eV in the Fe 2p spectrum can be assigned to the Ni auger peak [58, 59]. Further manifested by EELS analysis (Fig. 4(f)), the peaks at 705 and 730 eV represent respectively the Fe L-edge while the peaks at 850 and 875 eV elucidate the Ni L-edge, which emphasizes again the existence of Fe and Ni elements [60]. The high resolution of O 1s spectrum (Fig. 4(d)) is consisted of three fitted peaks denoted as O1-O3 (530.1, 531.6 and 533.5 eV), which are ascribed to Ni-Fe-O bonds, substituted hydroxyl groups, intrinsic oxygen vacancies on the surface, respectively [61]. The surface oxygen vacancies may be generated owing to compensating the deficit of positive charge caused by the reduction of Fe³⁺ to Fe²⁺ and the presence of Ni²⁺ in Oh sites [52]. Moreover, the high resolution of C 1s (Fig. 4(e)) can be deconvoluted into two peaks including 284.5 eV for C–C and 285.5 eV for C–O [43]. In view of all above, the peculiar inverse spinel structure of NiFe₂O₄ could be conducive to the catalytic activity by virtue of the huge active oxygen species on the surface vacancies.
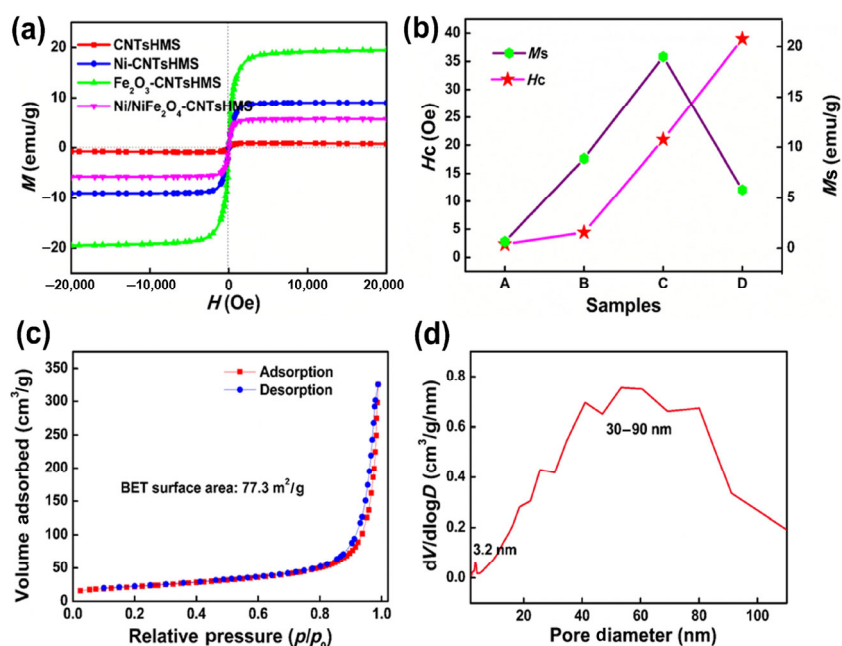
**Figure 3** Magnetic hysteresis loops (a) of CNTsHMS, Ni-CNTsHMS, Fe₂O₃-CNTsHMS and Ni/NiFe₂O₄-CNTsHMS at 300 K. The corresponding magnetic parameters (b) of CNTsHMS, Ni-CNTsHMS, Fe₂O₃-CNTsHMS and Ni/NiFe₂O₄-CNTsHMS. The nitrogen absorption/desorption isotherm (c) and the corresponding pore size distribution (d) of Ni/NiFe₂O₄-CNTsHMS.

Figure 5(a) shows the OER polarization curve at the potential window of 1.30–1.70 V (vs. RHE). The benchmark overpotentials at a current density of 10 mA/cm^2 (η_{10}) for Ni/NiFe$_2$O$_4$-CNTsHMS, Ni-CNTsHMS, and Fe$_2$O$_3$-CNTsHMS are estimated to be 1.541, 1.577 and 1.586 V, respectively. Figure 5(b) exhibits the related Tafel plots of catalysts to evaluate the OER kinetics. The Tafel slope for Ni/NiFe$_2$O$_4$-CNTsHMS is the smallest with 46.05 mV/dec (Fig. 5(b)) than others which are 118.45 mV/dec for CNTsHMS, 54.93 mV/dec for Fe$_2$O$_3$-CNTsHMS, and 50.86 mV/dec for Ni-CNTsHMS, respectively. In terms of η_{10} and Tafel slope, the Ni/NiFe$_2$O$_4$-CNTsHMS possesses the superior OER performance compared to Fe$_2$O$_3$-CNTsHMS, Ni-CNTsHMS, commercial RuO$_2$/IrO$_2$, and other non-noble metal nanocomposites (Fig. 5(c) and Table S4 in the ESM) [12, 18–24, 48–50, 62–65]. The EIS results (Fig. 5(d) and Table S5 in the ESM) further prove the favorable OER kinetics and fast catalytic rate for Ni/NiFe$_2$O$_4$-CNTsHMS because of smaller charge transfer resistance than others. To evaluate

their ECSA, the CV curves were performed in a small potential range of 1.225–1.275 V with various scan rates (4–20 mV/s) (Fig. S12 in the ESM). Obviously, the Ni/NiFe$_2$O$_4$-CNTsHMS has achieved the largest C_{dl} value (1.39 mF/cm^2) and ECSA value (3.41 cm^2), manifesting more exposed active sites (Fig. 5(c) and Fig. S13 in the ESM). Figure S14 in the ESM elucidates the ECSA-normalized LSV and Tafel plots of all CNTs self-supporting composites to explore the intrinsic activity of samples. Also, the Ni/NiFe$_2$O$_4$-CNTsHMS shows the lowest potential (1.30–1.57 V (vs. RHE)) and largest OER kinetics. Strikingly, in consideration of entire measured range from 1.30–1.70 V (vs. RHE), the ECSA-normalized LSV of Ni/NiFe$_2$O$_4$-CNTsHMS does not have an obvious advantage than Ni-CNTsHMS sample. To sum up, the hollow composite framework and heterojunction interface assembly more prefer to endow nanomaterial with the dominated active surface area and the accelerated kinetics. Moreover, the durability is another key factor to evaluate the catalytic performance of Ni/NiFe$_2$O$_4$-CNTsHMS. As shown in
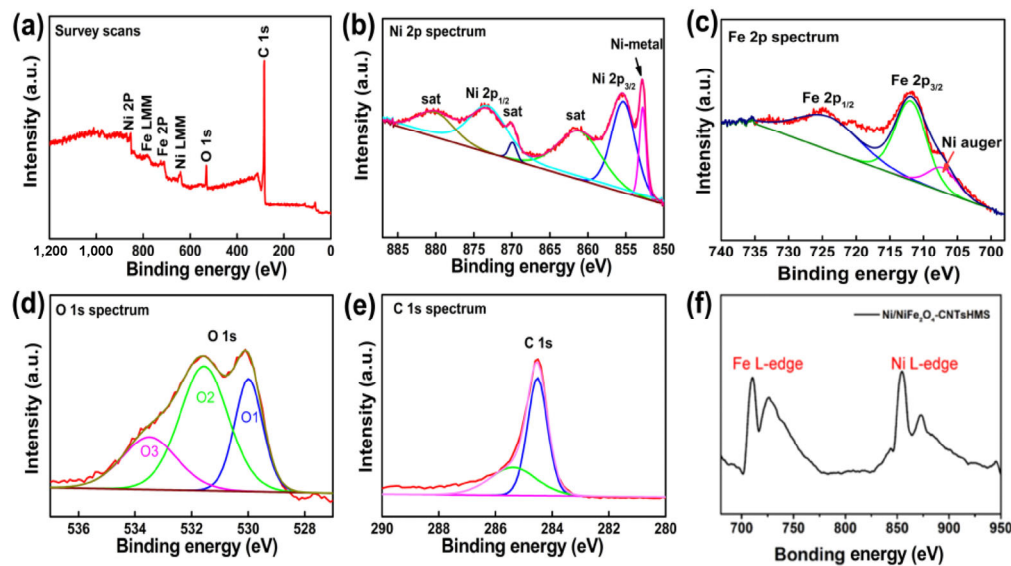
Figure 4 XPS spectra of Ni/NiFe$_2$O$_4$-CNTsHMS. (a) Wide scan, (b) Ni 2p spectrum, (c) Fe 2p spectrum, (d) O 1s spectrum, and (e) C 1s spectrum. (f) EELS spectrum of Ni/NiFe$_2$O$_4$-CNTsHMS.
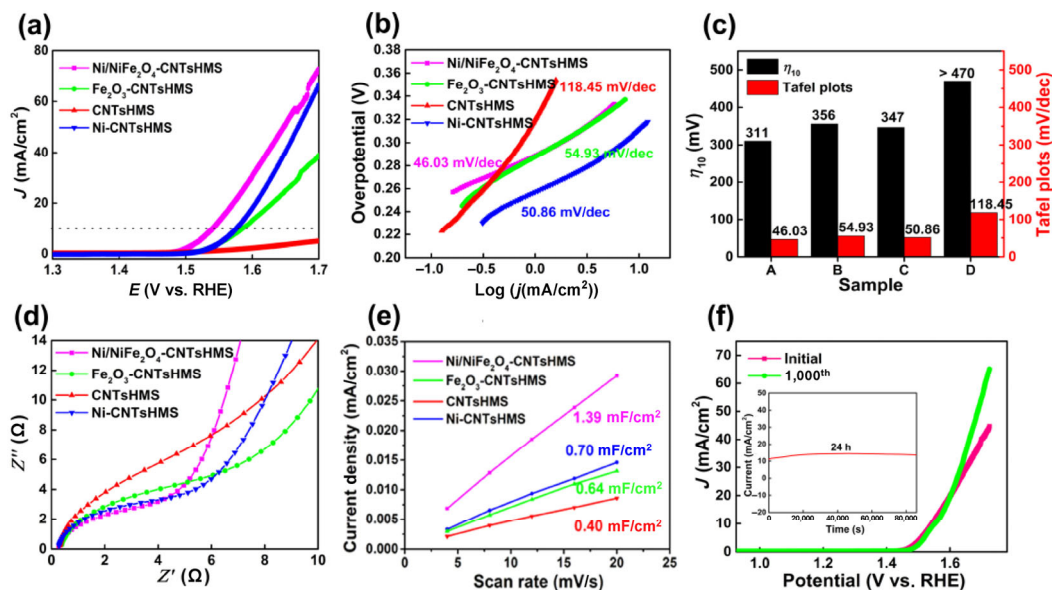
Figure 5 Electrochemical characterizations for OER. (a) Polarization curves. (b) Tafel plots. (c) The Electrochemical performance comparison for these samples: A Ni/NiFe$_2$O$_4$-CNTsHMS, B Fe$_2$O$_3$-CNTsHMS; C Ni-CNTsHMS; D CNTsHMS. (d) EIS spectra and (e) C_{dl} value of CNTsHMS, Ni-CNTsHMS, Fe$_2$O$_3$-CNTsHMS and Ni/NiFe$_2$O$_4$-CNTsHMS. (f) Polarization curves of Ni/NiFe$_2$O$_4$-CNTsHMS initially and after 1,000 CV cycles in 1 M KOH solution. The inset shows current density–time curve of Ni/NiFe$_2$O$_4$-CNTsHMS during OER.

Fig. 5(f), no distinct differences can be observed in current densities for Ni/NiFe$_2$O$_4$-CNTsHMS after 1,000 CV cycles. The inset current density–time curve also demonstrates the good stability of Ni/NiFe$_2$O$_4$-CNTsHMS sample during OER measurement. The favored stability is mainly contributed to the unique hierarchal structure. The activity nanoparticles are confined tightly onside the surface of hollow self-supporting CNTs shell, which prevents the active materials from dropping and decomposing.

Correspondingly, the XRD, SEM, and TEM characterizations after different OER durability test were carried out to research the structure and species changes of Ni/NiFe$_2$O$_4$-CNTsHMS sample. Observed on XRD data in Fig. S15 in the ESM, all exhibited peaks above can be perfectly ascribed to the NiFe$_2$O$_4$ competent (PDF#10-0325), indicating the durability properties of sample. Furthermore, the SEM (Fig. S16 in the ESM) and TEM images (Fig. S17 in the ESM) confirm there is no structural

evolution in this sample. The hollow 3D conductive framework is forcibly-assembled by 0D nanoparticle and 1D CNTs. In summary, the forcedly-assembled nanostructure of Ni/NiFe$_2$O$_4$-CNTsHMS by spray-drying is efficient for improving the conductivity and exposing more activity sites, thus accelerating the dynamic kinetics of oxygen evolution. In view of the facile synthesis and industrial outputs, the composites we fabricated is more convincing for further practical application.

To elucidate the correlation of interfacial charge distribution and the OER performance, the polarization charge density distribution of Ni/NiFe$_2$O$_4$-CNTsHMS was described by off-axis electron holography (Fig. 6). Reconstruction of the hologram images (Figs. 6(a)–6(e)), the phase shift (Θ) profiles of an electromagnetism (Figs. 6(a1)–6(e1)) can be further converted to electrostatic potential (V) according to the Poisson's equation [36, 66]. The conversion results of charge density curves were calculated in Figs. 6(a4)–6(c4) and 6(e2). As shown by Fig. 6(a4),
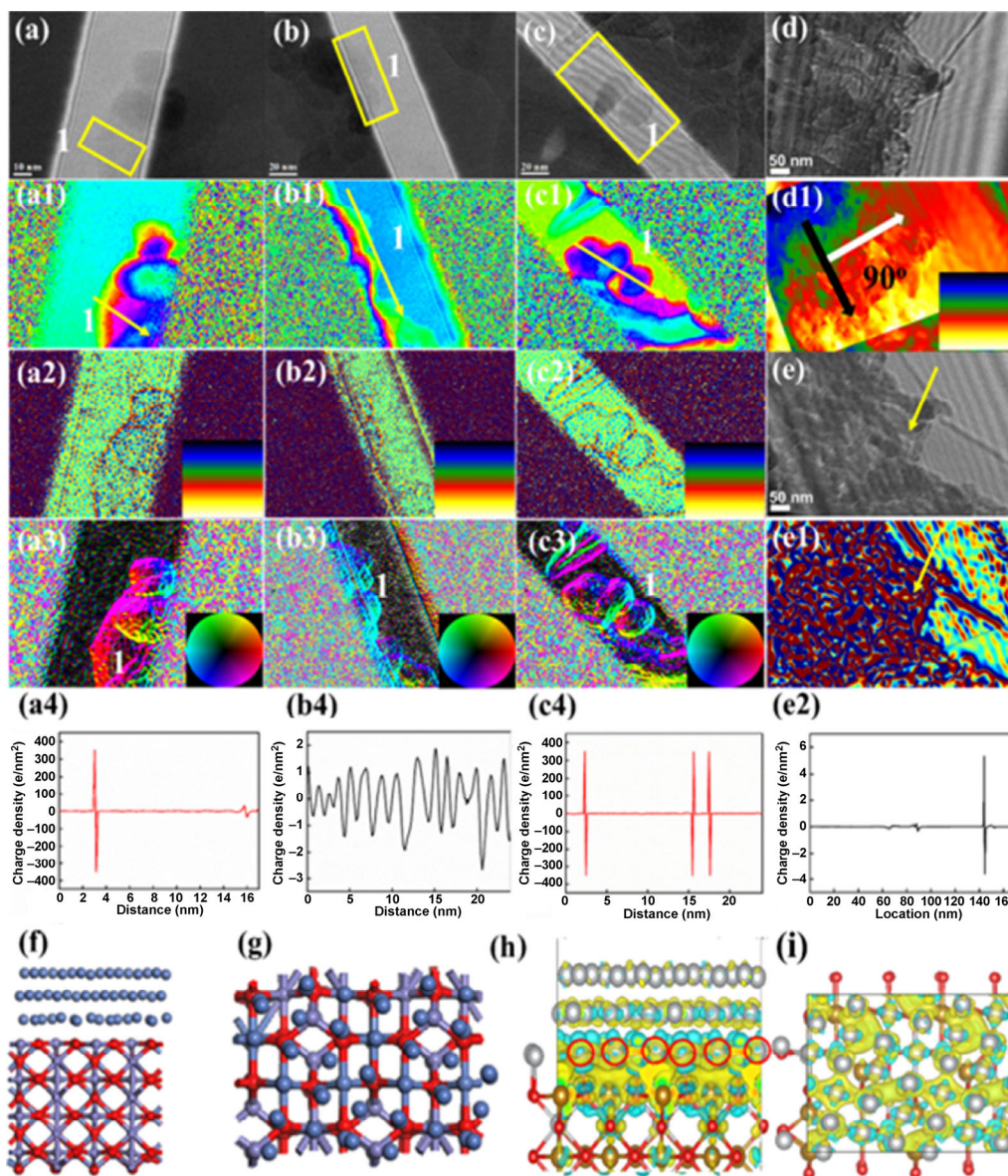
Figure 6 (a)–(c) Off-axis electron holograms; (a1)–(c1) reconstructed phase image; (a2)–(c2) charge density images; (a3)–(c3) electric field distribution images (the different color variations indicate the direction of the built-in electric field, and the intensity of same type color indicates the intensity of the built-in electric field). (a4)–(c4) The corresponding profile lines of charge density in the region of the yellow arrow. (d) Off-axis electron holograms. (d1) Reconstructed magnetic phase image (marked by black arrow) and the corresponding magnetic field direction (marked by white arrow). (e) Off-axis electron holograms (e1) charge density images (e2) the corresponding profile lines of charge density. The front view (f) and bottom view (g) of the optimized DFT calculation model of Ni/NiFe$_2$O$_4$ heterojunction interface. The front view (i) and bottom view (h) of differential charge density images by DFT calculation (the Ni atoms at the first floor epitaxial Ni were marked by red cycles).

the charge density distribution line profiles in the region of the yellow arrow (Figs. 6(a)and 6(a1)) exhibits strong charge redistribution at the interfaces of the CNTs. Notably, a large number of electrons have transported across CNTs, which facilitates the electron/charge conductivity by the adjustment of charge distribution. Figure 6(b4) depicts the corresponding line profiles of the polarization charge density distribution acquired from the two adjacent nanoparticles along the yellow arrow (Figs. 6(b) and 6(b1)). However, no strong charge redistribution happened at the interface of nanoparticles without the support of CNTs. These electrons have been evenly distributed onside the nanoparticle surface that could be attributed to the intrinsic electronics property of $NiFe_2O_4$ NPs. In comparison, when we take the interaction between NPs and CNTs into consideration (Figs. 6(c) and 6(c1) and Fig. S18 in the ESM), the interface synergistic effect can occur between NPs-NPs or NPs-CNTs (Fig. 6(c4) and Fig. S18 in the ESM). Figure 6(c4) reveals that the assistance of CNTs has extremely changed the electron distribution state onside the surface of nanoparticles, and results in strong charge polarization at the interface between NPs-NPs, which is always believed to the original of catalytic performance improvement. Similarly, the strengthening effect of CNTs also can take place by the interfacial heterojunction between CNTs-NPs (Fig. S18 in the ESM). The electrons have transferred along a direction from CNTs to nanoparticles. The intrinsic charge distribution of NPs can therefore be increased to enhance greatly the OER activity. Accordingly, a lot of built-in electric field is formed along with the heterojunction interfaces, which are the results of charge transfer (Figs. 6(a3)–(c3) in the ESM). On the other hand, we adopted a reversal phase technology to separately evaluate the static electrical and magnetic properties of the composite to investigate the electromagnetic coupling effect. Apparently, all the stray flux lines have completely penetrated through Ni/$NiFe_2O_4$-CNTsHMS. The strong magnetic field distribution from Ni/$NiFe_2O_4$ NPs (white arrow in Figs. 6(d) and 6(d1)) could influence the electron transfer of active sites by the Lorentz force [35, 36]. Moreover, Figs. 6(e) and 6(e2) exhibit similar polarization phenomenon between CNTs-NPs. Once again, it emphasizes the conductivity improvement effect of CNTs. To give insight to the affection of epitaxial Ni in Ni/$NiFe_2O_4$ NPs, the DFT calculation of charge-density difference has been carried out (Figs. 6(f)–6(i)). As a result, the electrons have been successfully accumulated at the oxygen sites in $NiFe_2O_4$ crystal lattice, accompanying with the electrons transferring out from Ni sites near the oxygen sites (Fig. 6(h)). Combined with the analysis of electron holography, a larger number of electrons from both CNTs and epitaxial Ni have migrated into $NiFe_2O_4$, which injects the assembled charge distribution into $NiFe_2O_4$. Therefore, the enriched electrons can weaken the Fe–O bonds of $NiFe_2O_4$ during the catalytic process, which can be more conducive to absorption/adsorption of OER intermediates [39–41]. Overall, by virtue of the hierarchal coupling and structure synergy, the composite conductivity and the intrinsic electrons distribution of $NiFe_2O_4$ NPs can be efficiently regulated, thereby boosting the OER catalytic kinetics.

Based on the above discussions, the OER catalytic improvement mechanisms for Ni/$NiFe_2O_4$-CNTsHMS are concluded (Fig. 7): i) A large number of surface defects are induced because of the peculiar inverse spinel structure of $NiFe_2O_4$ and conductive CNTs carrier itself, proven by XPS and Raman tests. These exposed defects could be intrinsically considered as active sites relating to the absorption/adsorption of OER intermediate. ii) Benefited from the hierarchical nanostructure, the 3D conductive framework assembled by 1D CNTs and 0D nanoparticles extremely improves the composite conductivity.
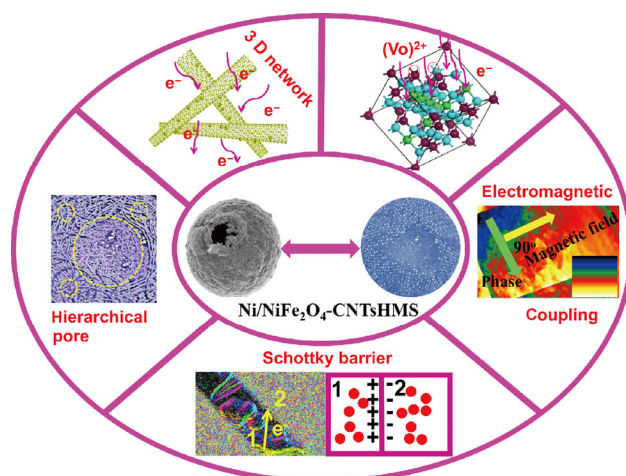
Figure 7 Schematic mechanism diagrams for oxygen evolution of Ni/$NiFe_2O_4$-CNTsHMS.

In addition, a large number of generated heterojunction interfaces promote the abundant electrons to transfer between CNTs-NPs and NPs-NPs manifested by off-axis electron holography. iii) The large surface area, the abundant nanopores and the smaller nanoparticle sizes are more favorable to expose more active sites, thus facilitating the mass transfer process of electrolytes. iv) The intrinsic magnetic field of Ni/$NiFe_2O_4$-CNTsHMS microsphere could influence the electron transportation of activity sites by Lorentz force. v) The further enriched electrons of $NiFe_2O_4$ by epitaxial Ni can weaken the Fe-O bonds during the catalytic process which is more beneficial for absorption/adsorption of OER intermediates. In short, due to the hierarchal coupling effects and synergy nanostructure, both conductivity and catalytic activity have been extremely improved. Therefore, the Ni/$NiFe_2O_4$-CNTsHMS microsphere exhibits an excellent OER performance better than the traditional NiFe-based oxide or commercial RuO_2/IrO_2.

4 Conclusions

In this work, we proposed a novel and facile spray-drying synthesis strategy for preparing the hollow Ni/$NiFe_2O_4$-CNTsHMS with industrial outputs. The unique nanostructure is assembled with a large number of Ni/$NiFe_2O_4$ NPs with less than 16 nm in diameter and the hollow CNTs self-supporting shell. Benefited from strong hierarchical coupling and optimized nanostructure synergy, both the conductivity and the catalytic activity of composite are greatly enhanced, which thus achieves the outstanding OER performance. Impressively, the overpotential at a current density of 10 mA/cm^2 has been optimized to 1.541 V (vs. RHE) with superior stability, which outperforms many reported catalysts based on other non-noble metal nanocomposites and commercial IrO_2/RuO_2. Confirmed by electron holography, the polarized heterojunction interfaces can improve extremely the conductivity and favors electron transportation from CNTs to $NiFe_2O_4$ NPs. Additionally, the intrinsic magnetic field of composite can affect the electron transportation paths of activity sites by the Lorentz force. The DFT calculation indicates that the intrinsic electron contents of $NiFe_2O_4$ can be further enriched from epitaxial Ni. Therefore, the Fe-O bonds of $NiFe_2O_4$ could be weakened during the catalytic process, which benefits absorption/adsorption of OER intermediates. This work hereby provides a simple and large-scale preparing strategy to design the hollow non-noble metal oxide/CNTs electrocatalysts and successfully reveals the enhanced mechanism of OER performance.

Acknowledgements

Electronic Supplementary Material: Supplementary material (computation details of differential charge density images in Ni/NiFe$_2$O$_4$ heterojunction interface; the syntheses schematic diagram of series of CNTs-based hollow microsphere; the enlargement XRD pattern and its corresponding HRTEM images of Fe$_2$O$_3$-CNTsHMS; the SEM/TEM images of series of CNTs-based hollow microsphere and the statistic histograms of the size distribution of Ni/NiFe$_2$O$_4$-CNTsHMS; the elements detection of Ni/NiFe$_2$O$_4$-CNTsHMS; the electrocatalytic performance of all CNTs-based samples which is compared with numerous no-noble metal nanocomposites) is available in the online version of this article at https://doi.org/10.1007/s12274-020-2626-y.

References

[1] Deng, S. J.; Zhong, Y.; Zeng, Y. X.; Wang, Y. D.; Wang, X. L.; Lu, X. H.; Xia, X. H.; Tu, J. P. Hollow TiO$_2$@Co$_9$S$_8$ core-branch arrays as bifunctional electrocatalysts for efficient oxygen/hydrogen production. *Adv. Sci.* (*Weinh*) **2018**, *5*, 1700772.

[2] Cheng, G. H.; Kou, T. T.; Zhang, J.; Si, C. H.; Gao, H.; Zhang, Z. H. O$_2^{2-}$/O$^-$ functionalized oxygen-deficient Co$_3$O$_4$ nanorods as high performance supercapacitor electrodes and electrocatalysts towards water splitting. *Nano Energy* **2017**, *38*, 155–166.

[3] Tang, C.; Wang, B.; Wang, H. F.; Zhang, Q. Defect engineering toward atomic Co-N$_x$-C in hierarchical graphene for rechargeable flexible solid Zn-air batteries. *Adv. Mater.* **2017**, *29*, 1703185.

[4] Si, C. H.; Zhang, Y. L.; Zhang, C. Q.; Gao, H.; Ma, W. S.; Lv, L. F.; Zhang, Z. H. Mesoporous nanostructured spinel-type MFe$_2$O$_4$ (M = Co, Mn, Ni) oxides as efficient bi-functional electrocatalysts towards oxygen reduction and oxygen evolution. *Electrochim. Acta* **2017**, *245*, 829–838.

[5] Li, P. S.; Duan, X. X.; Kuang, Y.; Li, Y. P.; Zhang, G. X.; Liu, W.; Sun, X. M. Tuning electronic structure of NiFe layered double hydroxides with vanadium doping toward high efficient electrocatalytic water oxidation. *Adv. Energy Mater.* **2018**, *8*, 1703341.

[6] Wang, Z.; Ang, J. M.; Zhang, B. W.; Zhang, Y. F.; Ma, X. Y. D.; Yan, T.; Liu, J.; Che, B. Y.; Huang, Y. Z.; Lu, X. H. FeCo/FeCoNi/N-doped carbon nanotubes grafted polyhedron-derived hybrid fibers as bifunctional oxygen electrocatalysts for durable rechargeable zinc–air battery. *Appl. Catal. B: Environ.* **2019**, *254*, 26–36.

[7] Jiang, H.; Gu, J. X.; Zheng, X. S.; Liu, M.; Qiu, X. Q.; Wang, L. B.; Li, W. Z.; Chen, Z. F.; Ji, X. B.; Li, J. Defect-rich and ultrathin N doped carbon nanosheets as advanced trifunctional metal-free electrocatalysts for the ORR, OER and HER. *Energy Environ. Sci.* **2019**, *12*, 322–333.

[8] Finke, C. E.; Omelchenko, S. T.; Jasper, J. T.; Lichterman, M. F.; Read, C. G.; Lewis, N. S.; Hoffmann, M. R. Enhancing the activity of oxygen-evolution and chlorine-evolution electrocatalysts by atomic layer deposition of TiO$_2$. *Energy Environ. Sci*, **2019**, *12*, 358–365.

[9] Zhen, D. X.; Zhao, B. T.; Shin, H. C.; Bu, Y. F.; Ding, Y.; He, G. H.; Liu, M. L. Electrospun porous perovskite La$_{0.6}$Sr$_{0.4}$Co$_{1-x}$Fe$_x$O$_{3-\delta}$ nanofibers for efficient oxygen evolution reaction. *Adv. Mater. Interfaces* **2017**, *4*, 1700146.

[10] Niu, S. Q.; Sun, Y. C.; Sun, G. J.; Rakov, D.; Li, Y. Z.; Ma, Y.; Chu, J. Y.; Xu, P. Stepwise electrochemical construction of FeOOH/Ni(OH)$_2$ on Ni foam for enhanced electrocatalytic oxygen evolution. *ACS Appl. Energy Mater.* **2019**, *2*, 3927–3935.

[11] Jin, H. Y.; Wang, J.; Su, D. F.; Wei, Z. Z.; Pang, Z. F.; Wang, Y. *In situ* cobalt-cobalt oxide/N-doped carbon hybrids as superior bifunctional electrocatalysts for hydrogen and oxygen evolution. *J. Am. Chem. Soc.* **2015**, *137*, 2688–2694.

[12] Mahala, C.; Sharma, M. D.; Basu, M. 2D nanostructures of CoFe$_2$O$_4$ and NiFe$_2$O$_4$: Efficient oxygen evolution catalyst. *Electrochim. Acta*

2018, *273*, 462–473.

[13] Li, T. F.; Lv, Y. J.; Su, J. H.; Wang, Y.; Yang, Q.; Zhang, Y. W.; Zhou, J. C.; Xu, L.; Sun, D. M.; Tang, Y. W. Anchoring CoFe$_2$O$_4$ nanoparticles on N-doped carbon nanofibers for high-performance oxygen evolution reaction. *Adv. Sci.* (*Weinh*) **2017**, *4*, 1700226.

[14] Yu, L.; Yang, J. F.; Guan, B. Y.; Lu, Y.; Lou, X. W. Hierarchical hollow nanoprisms based on ultrathin Ni-Fe Layered double hydroxide nanosheets with enhanced electrocatalytic activity towards oxygen evolution. *Angew. Chem., Int. Ed.* **2018**, *57*, 172–176.

[15] Zhou, D. J.; Cai, Z.; Lei, X. D.; Tian, W. L.; Bi, Y. M.; Jia, Y.; Han, N. N.; Gao, T. F.; Zhang, Q.; Kuang, Y. et al. NiCoFe-layered double hydroxides/N-doped graphene oxide array colloid composite as an efficient bifunctional catalyst for oxygen electrocatalytic reactions. *Adv. Energy Mater.* **2018**, *8*, 1701905.

[16] Zhao, S. L.; Li, M.; Han, M.; Xu, D. D.; Yang, J.; Lin, Y.; Shi, N. E.; Lu, Y. N.; Yang, R.; Liu, B. T. et al. Defect-rich Ni$_3$FeN nanocrystals anchored on N-doped graphene for enhanced electrocatalytic oxygen evolution. *Adv. Funct. Mater.* **2018**, *28*, 1706018

[17] Fu, G. T.; Cui, Z. M.; Chen, Y. F.; Li, Y. T.; Tang, Y. W.; Goodenough, J. B. Ni$_3$Fe-N doped carbon sheets as a bifunctional electrocatalyst for air cathodes. *Adv. Energy Mater.* **2017**, *7*, 1601172.

[18] Wang, W. H.; Yang, Y.; Huan, D. M.; Wang, L. K.; Shi, N.; Xie, Y.; Xia, C. R.; Peng, R. R.; Lu, Y. L. An excellent oer electrocatalyst of cubic SrCoO$_{3-\delta}$ prepared by a simple F-doping strategy. *J. Mater. Chem. A* **2019**, *7*, 12538–12546.

[19] Yue, X.; Jin, Y. S.; Shen, P. K. Highly stable and efficient non-precious metal electrocatalysts of tantalum dioxyfluoride used for the oxygen evolution reaction. *J. Mater. Chem. A* **2017**, *5*, 8287–8291.

[20] Li, M.; Lu, M. J.; Yang, J. R.; Xiao, J.; Han, L. N.; Zhang, Y. J.; Bo, X. J. Facile design of ultrafine CuFe$_2$O$_4$ nanocrystallines coupled porous carbon nanowires: Highly effective electrocatalysts for hydrogen peroxide reduction and the oxygen evolution reaction. *J. Alloys Compd.* **2019**, *809*, 151766.

[21] Han, M. N.; Shi, M. J.; Wang, J.; Zhang, M. L.; Yan, C.; Jiang, J. T.; Guo, S. H.; Sun, Z. Y.; Guo, Z. H. Efficient bifunctional Co/N dual-doped carbon electrocatalysts for oxygen reduction and evolution reaction. *Carbon* **2019**, *153*, 575–584.

[22] Wang, X.; Huang, X. K.; Gao, W. B.; Tang, Y.; Jiang, P. B.; Lan, K.; Yang, R. Z.; Wang, B.; Li, R. Metal–organic framework derived CoTe$_2$ encapsulated in nitrogen-doped carbon nanotube frameworks: A high-efficiency bifunctional electrocatalyst for overall water splitting. *J. Mater. Chem. A* **2018**, *6*, 3684–3691.

[23] Suryawanshi, U. P.; Suryawanshi, M. P.; Ghorpade, U. V.; Shin, S. W.; Kim, J.; Kim, J. H. An earth-abundant, amorphous cobalt-iron-borate (Co-Fe-B$_i$) prepared on Ni foam as highly efficient and durable electrocatalysts for oxygen evolution. *Appl. Surf. Sci.* **2019**, *495*, 143462.

[24] Liu, G.; Wang, K. F.; Gao, X. S.; He, D. Y.; Li, J. P. Fabrication of mesoporous NiFe$_2$O$_4$ nanorods as efficient oxygen evolution catalyst for water splitting. *Electrochim. Acta* **2016**, *211*, 871–878.

[25] He, K.; Tadesse Tsega, T.; Liu, X.; Zai, J. T.; Li, X. H.; Liu, X. J.; Li, W. H.; Ali, N.; Qian, X. F. Utilizing the space-charge region of the FeNi-LDH/CoP p-n junction to promote performance in oxygen evolution electrocatalysis. *Angew. Chem., Int. Ed.* **2019**, *58*, 11903–11909.

[26] Panda, C.; Menezes, P. W.; Yao, S. L.; Schmidt, J.; Walter, C.; Hausmann, J. N.; Driess, M. Boosting electrocatalytic hydrogen evolution activity with a NiPt$_3$@NiS heteronanostructure evolved from a molecular nickel-platinum precursor. *J. Am. Chem. Soc.* **2019**, *141*, 13306–13310.

[27] Xiong, Y.; Xu, L. L.; Jin, C. D.; Sun, Q. F. Interface-engineered atomically thin Ni$_3$S$_2$/MnO$_2$ heterogeneous nanoarrays for efficient overall water splitting in alkaline media. *Appl. Catal. B: Environ.* **2019**, *254*, 329–338.

[28] Guo, H. L.; Feng, Q. C.; Zhu, J. X.; Xu, J. S.; Li, Q. Q.; Liu, S. L.; Xu, K. W.; Zhang, C.; Liu, T. X. Cobalt nanoparticle-embedded nitrogen-doped carbon/carbon nanotube frameworks derived from a metal–organic framework for tri-functional ORR, OER and HER electrocatalysis. *J. Mater. Chem. A* **2019**, *7*, 3664–3672.

[29] Dong, C. Q.; Kou, T. Y.; Gao, H.; Peng, Z. Q.; Zhang, Z. H. Eutectic-derived mesoporous Ni-Fe-O nanowire network catalyzing oxygen evolution and overall water splitting. *Adv. Energy Mater.* **2018**, *8*, 1701347.

[30] Shan, J. Q.; Ling, T.; Davey, K.; Zheng, Y.; Qiao, S. Z. Transition-metal-doped RuIr bifunctional nanocrystals for overall water splitting in acidic environments. *Adv. Mater.* **2019**, *31*, 1900510.

[31] Andersen, N. I.; Serov, A.; Atanassov, P. Metal oxides/CNT nanocomposite catalysts for oxygen reduction/oxygen evolution in alkaline media. *Appl. Catal. B: Environ.* **2015**, *163*, 623–627.

[32] Li, Y. M.; He, H. Y.; Fu, W.; Mu, C. Z.; Tang, X. Z.; Liu, Z.; Chi, D. Z.; Hu, X. In-grown structure of NiFe mixed metal oxides and CNT hybrid catalysts for oxygen evolution reaction. *Chem. Commun. (Camb)* **2016**, *52*, 1439–1442.

[33] Zhang, X.; Zhang, X.; Wang, X. G.; Xie, Z. J.; Zhou, Z. NiFe₂O₄–CNT composite: An efficient electrocatalyst for oxygen evolution reactions in Li–O₂ batteries guided by computations. *J. Mater. Chem. A* **2016**, *4*, 9390–9393.

[34] Elizabeth, I.; Nair, A. K.; Singh, B. P.; Gopukumar, S. Multifunctional Ni-NiO-CNT composite as high performing free standing anode for Li ion batteries and advanced electro catalyst for oxygen evolution reaction. *Electrochim. Acta* **2017**, *230*, 98–105.

[35] Liu, Q. H.; Cao, Q.; Bi, H.; Liang, C. Y.; Yuan, K. P.; She, W.; Yang, Y. J.; Che, R. C. CoNi@SiO₂@TiO₂ and CoNi@Air@TiO₂ microspheres with strong wideband microwave absorption. *Adv. Mater.* **2016**, *28*, 486–90.

[36] Jiao, W. L.; Chen, C.; You, W. B.; Zhang, J.; Liu, J. W.; Che, R. C. Yolk-shell Fe/Fe₄N@Pd/C magnetic nanocomposite as an efficient recyclable ORR electrocatalyst and SERS substrate. *Small* **2019**, *15*, 1805032.

[37] Li, D. J.; Kang, J.; Lee, H. J.; Choi, D. S.; Koo, S. H.; Han, B.; Kim, S. O. High activity hydrogen evolution catalysis by uniquely designed amorphous/metal interface of core-shell phosphosulfide/N-doped CNTs. *Adv. Energy Mater.* **2018**, *8*, 1702806.

[38] Xia, W.; Mahmood, A.; Liang, Z. B.; Zou, R. Q.; Guo, S. J. Earth-abundant nanomaterials for oxygen reduction. *Angew. Chem., Int. Ed.* **2016**, *55*, 2650–2676.

[39] Li, Y. F.; Selloni, A. Mechanism and activity of water oxidation on selected surfaces of pure and Fe-doped NiOₓ. *ACS Catal.* **2014**, *4*, 1148–1153.

[40] Hong, D. C.; Yamada, Y.; Nagatomi, T.; Takai, Y.; Fukuzumi, S. Catalysis of nickel ferrite for photocatalytic water oxidation using [Ru(bpy)₃]²⁺ and S₂O₈²⁻. *J. Am. Chem. Soc.* **2012**, *134*, 19572–19575.

[41] Kumar, P. V.; Short, M. P.; Yip, S.; Yildiz, B.; Grossman, J. C. High surface reactivity and water adsorption on NiFe₂O₄ (111) surfaces. *J. Phys. Chem. C* **2013**, *117*, 5678–5683.

[42] Huang, X. P.; Pan, C. X.; Huang, X. T. Preparation and characterization of γ-MnO₂/CNTs nanocomposite. *Mater. Lett.* **2007**, *61*, 934–936.

[43] Yu, X. F.; Wang, L.; Liu, J. W.; Xue, S. Y.; Yang, L. T.; Li, X.; Zhang, J.; Xing, L. S.; Chen, G. Y.; Wang, M. et al. Ferromagnetic Co₂₀Ni₈₀ nanoparticles encapsulated inside reduced graphene oxide layers with superior microwave absorption performance. *J. Mater. Chem. C* **2019**, *7*, 2943–2953.

[44] Ye, F.; Song, Q.; Zhang, Z. C.; Li, W.; Zhang, S. Y.; Yin, X. W.; Zhou, Y. Z.; Tao, H. W.; Liu, Y. S.; Cheng, L. F. et al. Direct growth of edge-rich graphene with tunable dielectric properties in porous Si₃N₄ ceramic for broadband high-performance microwave absorption. *Adv. Funct. Mater.* **2018**, *28*, 1707205.

[45] Wang, H. F.; Tang, C.; Zhang, Q. A review of precious-metal-free bifunctional oxygen electrocatalysts: Rational design and applications in Zn-air batteries. *Adv. Funct. Mater.* **2018**, *28*, 1803329.

[46] Wang, C.; Han X. J.; Zhang, X. L.; Hu, S. R.; Zhang, T.; Wang, J. Y.; Du, Y. C.; Wang, X. H.; Xu, P. Controlled synthesis and morphology-dependent electromagnetic properties of hierarchical cobalt assemblies. *J. Phys. Chem. C* **2010**, *114*, 14826–14830.

[47] Wu, T.; Liu, Y.; Zeng, X.; Cui, T. T.; Zhao, Y. T.; Li, Y. N.; Tong, G. X. Facile hydrothermal synthesis of Fe₃O₄/C core-shell nanorings for efficient low-frequency microwave absorption. *ACS Appl. Mater. Interfaces* **2016**, *8*, 7370–7380.

[48] Chen, H.; Yan, J. Q.; Wu, H.; Zhang, Y. X.; Liu, S. Z. One-pot fabrication of NiFe₂O₄ nanoparticles on α-Ni(OH)₂ nanosheet for enhanced water oxidation. *J. Power Sources* **2016**, *324*, 499–508.

[49] Ma, Y. D.; Dai, X. P.; Liu, M. Z.; Yong, J. X.; Qiao, H. Y.; Jin, A. X.; Li, Z. Z.; Huang, X. L.; Wang, H.; Zhang, X. Strongly coupled FeNi alloys/NiFe₂O₄@carbonitride layers-assembled microboxes for enhanced oxygen evolution reaction. *ACS Appl. Mater. Interfaces* **2016**, *8*, 34396–34404.

[50] Li, M.; Xiong, Y. P.; Liu, X. T.; Bo, X. J.; Zhang, Y. F.; Han, C.; Guo, L. P. Facile synthesis of electrospun MFe₂O₄ (M = Co, Ni, Cu, Mn) spinel nanofibers with excellent electrocatalytic properties for oxygen evolution and hydrogen peroxide reduction. *Nanoscale* **2015**, *7*, 8920–8930.

[51] Zhao, Y.; Xu, L.; Yan, J.; Yan, W.; Wu, C. C.; Lian, J. B.; Huang, Y. P.; Bao, J.; Qiu, J. X.; Xu, L. et al. Facile preparation of NiFe₂O₄/MoS₂ composite material with synergistic effect for high performance supercapacitor. *J. Alloys Compd.* **2017**, *726*, 608–617.

[52] Feng, S. J.; Yang, W.; Wang, Z. B. Synthesis of porous NiFe₂O₄ microparticles and its catalytic properties for methane combustion. *Mater. Sci. Eng.: B* **2011**, *176*, 1509–1512.

[53] Chen, L. Y.; Dai, H.; Shen, Y. M; Bai, J. F. Size-controlled synthesis and magnetic properties of NiFe₂O₄ hollow nanospheres via a gel-assistant hydrothermal route. *J. Alloys Compd.* **2010**, *491*, L33–L38.

[54] Xu, K.; Ding, H.; Jia, K. C.; Lu, X. L.; Chen, P. Z.; Zhou, T. P.; Cheng, H.; Liu, S.; Wu, C. Z.; Xie, Y. Solution-liquid-solid synthesis of hexagonal nickel selenide nanowire arrays with a nonmetal catalyst. *Angew. Chem., Int. Ed.* **2016**, *55*, 1710–1713.

[55] Prieto, P.; Nistor, V.; Nouneh, K.; Oyama, M.; Abd-Lefdil, M.; Díaz, R. XPS study of silver, nickel and bimetallic silver–nickel nanoparticles prepared by seed-mediated growth. *Appl. Surf. Sci.* **2012**, *258*, 8807–8813.

[56] Nesbitt, H. W.; Legrand, D.; Bancroft, G.M. Interpretation of Ni₂P XPS spectra of Ni conductors and Ni insulators. *Phys. Chem. Miner.* **2000**, *27*, 357–366.

[57] Wang, X. Y.; Zhang, W. Z. Z.; Zhang, J. L.; Wu, Z. C. Fe-doped Ni₃S₂ nanowires with surface-restricted oxidation toward high-current-density overall water splitting. *ChemElectroChem* **2019**, *6*, 4550–4559.

[58] Wu, Z. C.; Wang, X.; Huang, J. S.; Gao, F. A Co-doped Ni–Fe mixed oxide mesoporous nanosheet array with low overpotential and high stability towards overall water splitting. *J. Mater. Chem. A* **2018**, *6*, 167–178.

[59] Wang, L. X.; Geng, J.; Wang, W. H.; Yuan, C.; Kuai, L.; Geng, B. Y. Facile synthesis of Fe/Ni bimetallic oxide solid-solution nanoparticles with superior electrocatalytic activity for oxygen evolution reaction. *Nano Res.* **2015**, *8*, 3815–3822.

[60] Mutz, B.; Sprenger, P.; Wang, W.; Wang, D.; Kleist, W.; Grunwaldt, J. D. *Operando* Raman spectroscopy on CO₂ methanation over alumina-supported Ni, Ni₃Fe and NiRh₀.₁ catalysts: Role of carbon formation as possible deactivation pathway. *Appl. Catal. A: Gen.* **2018**, *556*, 160–171.

[61] Li, Y. L.; Zhang, Z. Q.; Pei, L. Y.; Li, X. G.; Fan, T.; Ji, J.; Shen, J. F.; Ye, M. X. Multifunctional photocatalytic performances of recyclable Pd-NiFe₂O₄/reduced graphene oxide nanocomposites via different co-catalyst strategy. *Appl. Catal. B: Environ.* **2016**, *190*, 1–11.

[62] Liu, G.; Gao, X. S.; Wang, K. F.; He, D. Y.; Li, J. P. Uniformly mesoporous NiO/NiFe₂O₄ biphasic nanorods as efficient oxygen evolving catalyst for water splitting. *Int. J. Hydrogen Energy* **2016**, *41*, 17976–17986.

[63] Wang, X. M.; Zhang, H.; Yang, Z.; Zhang, C.; Liu, S. X. Ultrasound-treated metal-organic framework with efficient electrocatalytic oxygen evolution activity. *Ultrason. Sonochem.* **2019**, *59*, 104714.

[64] Balogun, M. S.; Qiu, W. T.; Yang, H.; Fan, W. J.; Huang, Y. C.; Fang, P. P.; Li, G. R.; Ji, H. B.; Tong, Y. X. A monolithic metal-free electrocatalyst for oxygen evolution reaction and overall water splitting. *Energy Environ. Sci.* **2016**, *9*, 3411–3416.

[65] Fang, Z. Q; Hao, Z. M.; Dong, Q. S.; Cui, Y. Bimetallic NiFe₂O₄ synthesized via confined carburization in NiFe-MOFs for efficient oxygen evolution reaction. *J. Nanopart. Res.* **2018**, *20*, 106.

[66] Liu, H. D.; Chen, Z. L.; Zhou, L.; Li, X.; Pei, K.; Zhang, J.; Song, Y.; Fang, F.; Che, R. C.; Sun, D. L. Rooting bismuth oxide nanosheets into porous carbon nanoboxes as a sulfur immobilizer for lithium-sulfur batteries. *J. Mater. Chem. A* **2019**, *7*, 7074–7081.